Composites Part B 283 (2024) 111637

Contents lists available at ScienceDirect

Composites Part B

journal homepage: www.elsevier.com/locate/compositesb

MOF-derived metal oxide (Cu, Ni, Zn) gas sensors with excellent selectivity towards H_2S, CO and H_2 gases

Carmen Montoro [a,b,1], Jin-Young Kim [c,1], Ali Mirzaei [d], Jae-Hyoung Lee [c], Syreina Sayegh [e], Elissa Makhoul [e], Igor Iatsunskyi [f], Emerson Coy [f], Mikhael Bechelany [e,g,*], Hyoun Woo Kim [h,**], Sang Sub Kim [c,***]

[a] Department of Inorganic Chemistry, Autonomus University of Madrid, 28049, Madrid, Spain
[b] Institute for Advanced Research in Chemical Sciences (IAdChem), Universidad Autónoma de Madrid, 28049, Madrid, Spain
[c] Department of Materials Science and Engineering, Inha University, Incheon, 22212, Republic of Korea
[d] Department of Materials Science and Engineering, Shiraz University of Technology, Shiraz, 715557-13876, Islamic Republic of Iran
[e] Institut Européen des Membranes, IEM, UMR 5635, Univ Montpellier, ENSCM, CNRS, Montpellier, France
[f] NanoBioMedical Centre, Adam Mickiewicz University, Wszechnicy Piastowskiej 3, 61-614, Poznan, Poland
[g] Gulf University for Science and Technology, GUST, Kuwait
[h] Division of Materials Science and Engineering, Hanyang University, Seoul, 04763, Republic of Korea

ARTICLE INFO

Keywords:
MOF-Derived metal oxide
CuO
ZnO
NiO
Gas sensor
Selectivity
Sensing mechanism

ABSTRACT

Metal-organic framework (MOF)-derived metal oxides blend the sensing properties of metal oxides with MOF porosity, enhancing gas sensing capabilities. In this study, M-MOFs (M = Cu, Ni and Zn) were synthesized and then calcined at different temperatures to obtain their corresponding metal oxides (CuO, NiO and ZnO). The synthesis method incorporated novel approaches to enhance sensor performance, such as optimizing calcination temperatures for improved selectivity. Structural and morphological analyses confirmed the high surface area and porosity of the metal oxide materials, facilitating efficient gas adsorption and promoting enhanced sensor response. Gas sensing studies revealed significantly enhanced performance of MOF-derived metal oxides over M-MOFs, strongly influenced by calcination temperature. Moreover, CuO, NiO and ZnO MOF-derived metal oxides showed improved selectivity towards H_2S, CO and H_2 gases, respectively. This study demonstrates that tuning MOF and calcination parameters can tailor sensor selectivity effectively.

1. Introduction

Hydrogen (H_2) is an important gas and has a wide range of applications in different industries, such as food processing, medical treatments, aerospace, and energy storage. It is also one of the cleanest and most environmentally friendly sustainable energy sources due to its abundance, cleanliness, and recyclability [1–3]. Furthermore, H_2 monitoring in exhaled breath can be used as a gauge to examine intestinal conditions. For instance, a hydrogen breath test is widely used to diagnose small intestinal bacterial overgrowth syndrome and carbohydrate (fructose, lactose, and sorbitol) malabsorption [4]. However, it is a highly explosive gas (4–75 vol%) with high combustion heat (142 kJ g^{-1}), low ignition energy (0.02 mJ), and high flame propagation velocity [5]. In case of leakage, which is facilitated by H_2 small molecule size (0.289 nm) and high diffusion coefficient (0.61 cm^2/s), the risk of disasters is high [6]. Unfortunately, H_2 gas leakages cannot be easily detected due to H_2 absence of color, odor and taste [7]. Hence, reliable H_2 gas sensors with high sensitivity and robustness are needed to avoid leakage-related accidents and explosions [8].

H_2S gas is a colorless, corrosive, water-soluble, highly toxic, and flammable gas in the range of 4–44 vol% with an unpleasant rotten egg-like smell. At low concentrations, it is highly irritant to eyes, skin, nose and throat and at concentrations above 100 ppm, it paralyzes the olfactory nerves, and the sense of odor disappears, which gives the false

* Corresponding author. Institut Européen des Membranes, IEM – UMR 5635, Univ Montpellier, ENSCM, CNRS, Montpellier, France.
** Corresponding author. Division of Materials Science and Engineering, Hanyang University, Seoul, 04763, Republic of Korea.
*** Corresponding author. Department of Materials Science and Engineering, Inha University, Incheon, 22212, Republic of Korea.
E-mail addresses: mikhael.bechelany@umontpellier.fr (M. Bechelany), hyounwoo@hanyang.ac.kr (H.W. Kim), sangsub@inha.ac.kr (S.S. Kim).
[1] Both contribute equally to this paper.

https://doi.org/10.1016/j.compositesb.2024.111637
Received 22 March 2024; Received in revised form 18 May 2024; Accepted 15 June 2024
Available online 15 June 2024

impression that exposure to the gas was finished. At concentrations higher than 1000 ppm it can be lethal [9,10]. In addition, H_2S is a known biomarker for Down syndrome, Alzheimer's disease, ischemia, asthma, and halitosis [11] Therefore, reliable detection of H_2S is also of importance.

CO is odorless, tasteless and colorless with a highly toxic nature, which is mainly emitted from the incomplete burning of fossil fuels. It is known as the silent killer and since human red blood cell hemoglobin (Hb) is a major target site for CO, it combines with hemoglobin to form carboxyhemoglobin, a molecule that is incapable of carrying oxygen to tissue sites, resulting in tissue hypoxia [12,13]. Nausea, headache and dizziness are observed with CO-Hb levels over 10 %, and when the amount of CO-Hb increases to 30–50 %, severe health issues like increases in respiratory and heart rates, syncope, motor paralysis and confusion are observed. In higher levels of poisoning death is likely [14]. Therefore, reliable detection of CO gas is also vital from our safety point of view.

Different H_2 gas sensors, such as electrochemical [15], catalytic [16], optical [17], surface acoustic wave [18], metallic thin film [19], gasochromic [20] and resistive-based sensors [21], have been developed. Also, various gas sensors for the detection of CO and H_2S gases have been reported in the literature [22–27]. Resistive gas sensors, which rely on semiconducting metal oxides (SMO), such as SnO_2 [28], In_2O_3 [29], ZnO [30], NiO [31], and CuO [32] display good response and stability, fast dynamics, small size, simple operation and low price [33]. However, in their pristine form, they generally show poor selectivity towards a specific gas.

Metal-organic frameworks (MOFs) are porous materials in which metal clusters and organic ligands are connected through coordination bonds [34]. Due to their high specific surface area, tunability and high stability, they are ideal materials for potential applications such as gas adsorption and separation [35], drug delivery [36], gas sensors [37], water treatment [38], catalysis [39] and energy storage [40]. MOFs can also be used as precursors for the preparation of different functional nanostructures (*i.e.* SMOs) [41] that are exploited in many different fields, including electrochemical energy storage [42], catalysis [43] and sensing [44]. Specifically, MOF-derived SMOs have been used as electrically-transduced gas sensors, such as chemiresistors, chemicapacitors and electrochemical gas sensors [45–49].

However, control of high temperature pyrolysis procedure is one of most challenging issues to successfully maintain the original high porosity and surface areas of MOFs, so that the MOF-derived materials could achieve excellent performance as gas sensor [50].

Several groups have investigated the use of MOFs and the derived SMOs for gas detection due to their large specific surface area, tunable pore sizes, low density, and ordered crystal structure. For instance, Nguyen et al. tested Co-MOF-74, Ni-MOF-74 and Mg-MOF-74 and found that Co-MOF-74 was the best H_2 gas sensor due to the presence of two oxidation Co states (+2 and + 3) in the cluster [51]. Also, regarding CO gas sensing by MOFs, Nguyen et al. [52], reported fabrication of a Ni-incorporated MOF gas sensor. However, it showed a low response of only 1.7–50 ppm CO gas. Aykanat et al. [53], reported MOFs with metallophthalocyanine (MPc, M = Co and Ni) units for CO gas sensing. Surya et al. [54] reported Ag-decorated UiO-66 (Zr) MOF-based capacitive sensor for the detection of H_2S gas. However, overall, MOF gas sensors have poor sensing performance due to their low conductivity and stability.

However, overall, MOF gas sensors have poor sensing performance due to their low conductivity and stability. However, MOFs, in combination with metal oxides show promising sensing properties. For example, Drobek et al. increased the selectivity of pristine ZnO nanowires by growing a thin layer of zeolitic imidazolate frameworks (ZIF)-8 onto the nanowire surface. This led to a response of 1.44–50 ppm H_2 gas at 300 °C and a very small response to other gases, such as toluene and benzene [55]. Following a similar approach, Weber et al. combined ZnO nanowires decorated with Pd nanoparticles (NPs) and ZIF-8 as porous material. This led to a response of 9–50 ppm H_2 gas at 200 °C. The addition of Pd NPs increased the electron depletion layer depth at the Pd–ZnO contact area, leading to higher resistance than with the ZnO NW sensor. In the presence of H_2 gas, Pd and part of the ZnO surface were converted into PdH_x and metallic Zn, respectively, which contributed to the increase in the conductivity, influencing the sensor response [56].

Interestingly, MOFs can be easily transformed into SMOs with a large surface area and controlled shape by using the appropriate heat treatment [57,58]. In fact, MOF-derived SMOs combine the good intrinsic sensing properties of metal oxides and the highly porous structure of MOFs, which can boost the sensing performance [59]. For example, DMello et al. recently reported the preparation of a MOF-derived Co–ZnO gas sensor anchored on nitrogen-doped carbon that could detect H_2 (1 % of concentration) at room temperature [60]. Hussain et al. reported enhanced sensitivity of CuO-decorated ZnO polyhedral nanostructures towards H_2S gas [61]. In another study, Chen and co-workers, reported MOF-derived Co_3O_4 NPs over direct grown ZnO nanoflowers for selective sensing of CO gas [62].

In this work, to tune the selectivity of MOF-derived SMOs towards different gases, we synthesized three different MOFs based on Cu, Ni and Zn metals and their nanostructured SMOs counterparts (*i.e.* CuO, NiO and ZnO) by calcination in air at different temperatures (400, 500 and 600 °C). The gas sensing test results showed enhanced sensing performance of MOF-derived CuO, NiO and ZnO compared with their original MOF counterparts. Furthermore, the three MOF-derived SMO gas sensors showed improved selectivity towards H_2S, CO and H_2 gases, respectively. Therefore, the selectivity of the resulting SMO gas sensor can be finely adjusted through the strategic selection of MOF precursors and specific calcination temperatures. Our study introduces a fresh perspective by investigating how variations in calcination temperatures influence the gas sensing properties of MOF-derived metal oxides, thus improving their practical utility.

2. Experimentation

2.1. Materials

All used chemicals were commercially available and were used as purchased. The chemicals 4-carboxypyrazole (4-cpz, 95 %), 1,4-benzenedicarboxylic (1,4-bdc, 97 %), 1,4-diazabicyclo [2.2.2] octane (DABCO, ≥99 %), copper nitrate trihydrate ($Cu(NO_3)_2{\cdot}3H_2O$, ≥99 %), nickel acetate tetrahydrate ($Ni(AcO)_2{\cdot}4H_2O$, ≥99 %), zinc nitrate hexahydrate ($Zn(NO_3)_2{\cdot}6H_2O$, ≥99 %) were from Merck. The solvents *N,N*-dimethylformamide (DMF, ≥99 %), ethanol (≥99 %), diethyl ether (≥99 %) and dichloromethane (DCM, ≥99 %) were from Fisher Scientific.

2.2. MOF and MOF-derived SMO synthesis

$NH_4[Cu_3(\mu_3\text{-}OH)(\mu_3\text{-}4\text{-}cpz)_3]$, (Cu-MOF) was obtained following a previously described procedure [63]. Briefly, 222 mg 4-cpz (2 mmol) and 480 mg $Cu(NO_3)_2{\cdot}3H_2O$ (2 mmol) were dissolved in 30 mL of an aqueous ammonia solution (1:15, NH_3/H_2O) giving rise to a blue solution. After incubation for 3 days, the obtained dark blue crystals were filtered and rinsed in ethanol and diethyl ether. Before use, crystals were reduced to powder in an agate mortar.

$[Ni_8(OH)_4(H_2O)_2(cpz)_6]$, (Ni-MOF) was synthesized using the approach described in [64]. After dissolving 33.3 mg 4-cpz (0.3 mmol) in 16 mL DMF and 99.2 mg $Ni(AcO)_2{\cdot}4H_2O$ (0.4 mmol) in 4 mL H_2O, they were mixed for 6 h. The obtained green solid was filtered, rinsed in ethanol and diethyl ether, followed by DMF exchange with DCM.

$[Zn_2(bdc)_2(dabco)]$ (Zn-MOF) was obtained following a previously described protocol [65]. After dissolution of 500 mg $Zn(NO_3)_2{\cdot}6H_2O$ (1.68 mmol) and 280 mg 4-bdc (1.68 mmol) in 14 mL DMF and 0.0935 mg DABCO (0.84 mmol) in 6 mL DMF, the two solutions were stirred at 120 °C for 48 h. The product was washed with DMF and DCM.

The obtained Cu-, Ni- and Zn-MOFs were then calcined at 400, 500, 600 °C in air for 2 h to obtain porous nanostructured CuO, NiO and ZnO, respectively.

2.3. Gas sensor fabrication

Photolithography and SiO_2–Si (100) were used to fabricate bi-layered and patterned-interdigital electrodes. A Ti (~50 nm) layer was deposited to improve the adhesion between the SiO_2 substrate and electrode, and Pt (~200 nm) was used as electrode. To prepare the gas sensors, 10 mg of the synthesized MOFs and MOF-derived SMOs in powder form and 0.5 μL α-terpineol were mixed in a mortar and the obtained paste was coated onto the electrode layer and dried at 70 °C in air for 1 h. The obtained gas sensors were annealed at 350 °C for 1 h to remove the organic species and stabilize their baseline electrical resistance. The thickness of sensing layer over the substrate was ~6 μm (Fig. S1).

2.4. Gas sensing measurements

The fabricated gas sensors were put into a gas chamber inside a horizontal tubular furnace with possible temperature control. In the chamber, the concentration of the gas to be tested was obtained by adjusting the gas and dry air ratio using mass flow controllers (total flow rate = 500 sccm). Each sensor response was calculated using $R=R_a/R_g$ or $R=R_g/R_a$, in function of the sensor type and tested gas, where R_g and R_a were the resistance in the presence of gas and air, respectively. The response time and recovery time were defined as the times needed to reach 90 % of the change in resistance after injection and removal of the tested gas, respectively.

2.5. Characterizations

Shape and elemental composition were characterized using scanning electron microscopy (SEM; Hitachi S4800 microscope, Japan), transmission electron microscopy (TEM; JEOL 2200FS, 200 kV, and JEOL ARM-200F, 200 kV) and energy-dispersive X-ray (EDX) spectroscopy (Zeiss EVO HD15 microscope with an Oxford X-MaxN EDX detector). The crystal phases were determined by X-ray diffraction (XRD; PAN-Alytical Xpert-PRO diffractometer) using Cu-$K_{\alpha 1}$ radiation ($\lambda = 1.5406$ Å) and a 2θ range from 10 to 80°. Raman spectra were measured by dispersive Raman spectroscopy (Horiba XploRA), using a 659.55 nm laser and a 100x objective. The surface elemental composition and the different surface areas were assessed by X-ray photoelectron spectroscopy (XPS) with a monochromatic X-ray source (Al-Kα; $h\nu = 1486.6$ eV) and by N_2 adsorption-desorption at 77 K. For elemental mapping, a Zeiss EVO HD15 microscope and an Oxford X-MaxN energy-dispersive X-ray (EDS) detector was used.

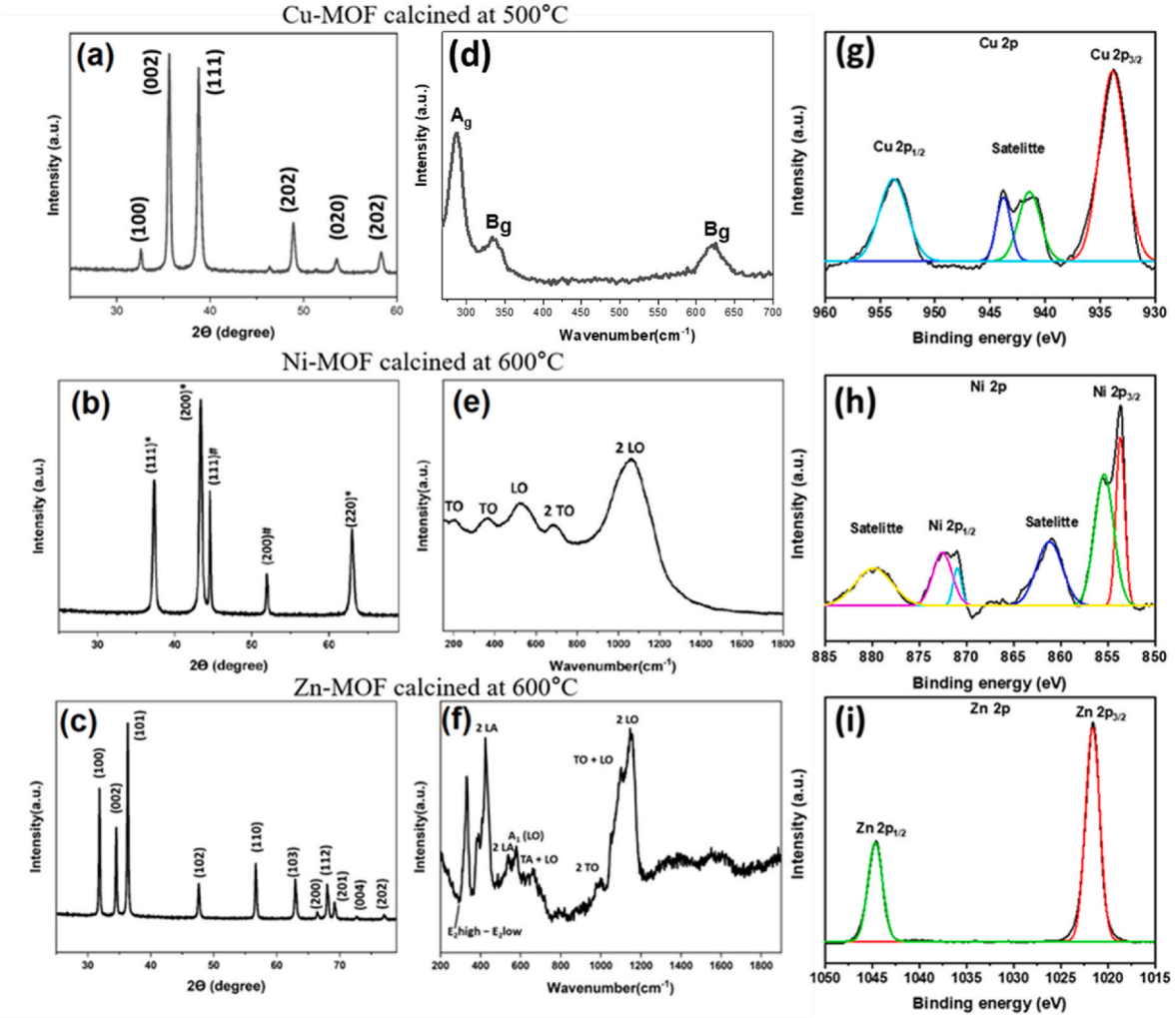

Fig. 1. XRD patterns of (a) Cu-MOF (b) Ni-MOF and (c) Zn-MOF materials calcined in air at 500, 600 and 600 °C, respectively. Raman spectra of (d) Cu-MOF (e) Ni-MOF and (f) Zn-MOF materials calcined in air at 500, 600 and 600 °C, respectively. XPS core-level spectra of (g) Cu 2p for Cu-MOF after calcination at 500 °C, (h) Ni 2p for Ni-MOF after calcination at 600 °C, and (i) Zn 2p for Zn-MOF after calcination at 600 °C.

3. Results and discussion

3.1. Morphological and structural analyses

The Cu- and Ni-MOFs were based on the same pyrazolate organic ligand, while the Zn-MOF was based on the 4-bdc and DABCO organic ligands. Then, these MOFs were calcined to obtain oxide-based materials, the structure of which was assessed by XRD and Raman measurements. XRD analysis of MOF-derived CuO (obtained by calcination at 500 °C) (Fig. 1a) highlighted sharp peaks at 32.6°, 35.6°, 38.7°, 48.9°, 53.5°and 58.3° that were assigned to the (100), (002), (111), (202), and (020) crystalline planes of single phase monoclinic CuO (JCPDS Card No.48-1548), respectively. No peak related to impurities, such as Cu, Cu_2O or $Cu(OH)_2$, was detected, implying the successful synthesis and high purity of the starting materials. The XRD analysis of MOF-derived NiO (calcination at 600 °C) (Fig. 1b) highlighted diffraction peaks at 37.4°, 43.4°, and 63.0° that were assigned to the (111), (200) and (220) crystalline planes of NiO with NaCl structure (JCPDS Card No. 47–1049), respectively [66,67]. Two other diffraction peaks at 44.6° and 51.9° were observed, suggesting the presence of the Ni_2O_3 phase due to calcination in air. The XRD analysis of MOF-derived ZnO (calcined at 600 °C) (Fig. 1c) showed that all peaks matched the typical Wurtzite crystal structure of ZnO (JCPDS No. 36–1451) [68,69]. Moreover, the absence of other peaks demonstrated the successful formation of a pure ZnO phase.

Similarly, Raman measurements were carried out after calcination at 500 °C (Cu-MOF) and 600 °C (Ni-MOF and Zn-MOF). Cu-MOF (Fig. 1d) displayed one peak at 285 cm^{-1} (assigned to the Ag mode of the CuO phase) and two peaks at 333 and 620 cm^{-1} (assigned to the B_g modes of the CuO phase) [70,71], in agreement with previous studies. In the Ni-MOF Raman spectrum (Fig. 1e), five Raman peaks at 210, 370, 530, 690 and 1055 cm^{-1} were observed. The peaks at ~200 and 370 cm^{-1} and the peak at 530 cm^{-1} corresponded to the first order transverse optical (TO) and to the longitudinal optical (LO) phonon modes of NiO, respectively. The peaks at 700 and 1055 cm^{-1} were assigned to the 2TO and 2LO combinations, respectively [72,73]. All Zn-MOF peaks (Fig. 1f) matched those described in the literature and the peak at ~1144 cm^{-1} contained contributions from $2A_1$(LO) and $2E_1$(LO) [68]. The first- and second-order Raman modes, due to ZnO monocrystals, were in line with the XRD findings. Then, XPS was used to obtain more information on the chemical compositions and states after calcination. The high-resolution Cu 2p spectra for Cu-MOF (obtained by calcination at 500 °C) displayed the specific Cu $2p_{3/2}$ (933.9 eV) and Cu $2p_{1/2}$ (953.6 eV) peaks and also satellite peaks, from 941.4 to 943.7 eV, indicative of Cu^{2+} presence (Fig. 1g). This confirmed the XRD results and the successful synthesis of CuO without any impurity, such as Cu, Cu_2O or $Cu(OH)_2$. The high-resolution Ni 2p spectra of Ni-MOF (obtained by calcination at 600 °C) (Fig. 1h) included binding peaks (~851.7 and 872.1 eV), assigned to Ni $2p_{3/2}$ and Ni $2p_{1/2}$ respectively, and satellite peaks (861.1 and 879.7 eV). Deconvolution revealed that the Ni $2p_{3/2}$ and Ni $2p_{1/2}$ peaks included two peaks/each: two peaks at 853.7 and 871.0 eV (assigned to Ni^{2+}, confirming NiO synthesis) and two peaks at 855.5 and 872.5 eV (assigned to Ni^{3+} [74,75] indicating Ni_2O_3 formation during calcination in air). The high-resolution Zn 2p spectra for Zn-MOF after calcination at 600 °C revealed binding peaks at ~1021.6 and 1044.7 eV, corresponding to Zn $2p_{3/2}$ and Zn $2p_{1/2}$, respectively (Fig. 1i). This strongly suggests the presence of zinc ions in a divalent state (Zn^{2+}) [76,77], in line with the ZnO phase observed by XRD. Fig. S2 shows the high-resolution O1s and C1s spectra. The deconvolution of the C1s spectrum revealed three peaks that corresponded to the C═C bond of phenyl carbons, the C–O bond, and the C═O bond. This indicated that residual carbon was still present in all samples. The O1s region of all samples was fitted in two curves related to lattice oxygen (O-M) and adsorbed oxygen (–OH), in accordance with the literature. The peaks at 529.6, 529.2, and 530.1 eV were assigned to Cu–O, Ni–O, and Zn–O bonds, respectively.

SEM and TEM analysis were employed to investigate the morphology and microstructure of the materials. Then, MOF-derived CuO after calcination at 500 °C showed the presence of some agglomerations among NPs (SEM; Fig. 2a) and of spherical NPs with a mean size of ~50–60 nm (TEM; Fig. 2b). High-resolution (HR)-TEM analysis indicated that the inter-planar lattice distance was 0.22 nm, which belongs to the (111) crystal plane of CuO (Fig. 2c). Similarly, SEM and TEM analysis of the MOF-derived NiO (calcined at 600 °C) showed some agglomeration among NPs (SEM; Fig. 2d) and the presence of NiO NPs of almost spherical shape with a mean size of ~25 nm (TEM; Fig. 2e). HR-TEM (Fig. 2f) revealed an inter-planar lattice distance of 0.23 nm, which belongs to the (002) crystal plane of NiO [78,79]. MOF-derived ZnO (calcined at 600 °C) was composed of small interconnected NPs with homogeneous size (SEM; Fig. 2g), in line with previous results [80]. The ZnO NPs were almost spherical with a mean size of ~35–45 nm (TEM; Fig. 2h). The inter-planar lattice distance was 0.24 nm, which belongs to the (101) crystal plane of ZnO (HR-TEM; Fig. 2i).

The elemental composition was assessed by EDS (Table 1). In MOF-derived CuO (calcined at 500 °C), the concentrations of Cu and O elements were 76.9 and 23.1 wt%, respectively. In MOF-derived NiO (calcined at 600 °C), Ni and O elements represented 77.3 and 22.7 wt%, respectively. In MOF-derived ZnO (calcined at 600 °C), Zn and O elements were 79.1 and 20.9 wt%, respectively.

The N_2 adsorption-desorption curves of the different samples are in Fig. 3. The BET surface areas of MOF-derived CuO (calcined at 500 °C), NiO (calcined at 600 °C), and ZnO (calcined at 600 °C) were 5.48, 12.65, and 8.36 m^2/g, respectively. Therefore, NiO had the highest surface area.

3.2. Gas sensing studies

3.2.1. Gas sensors based on Cu-MOF and Cu-MOF-derived CuO

After exposure to 1, 5 and 10 ppm H_2S gas (a reducing gas) at 100, 150 and 200 °C, the Cu-MOF gas sensor resistance increased (Fig. 4a). This indicates that Cu-MOF behaves like a p-type sensor. Conversely, the baseline resistance was decreased by the sensing temperature, highlighting Cu-MOF semiconducting nature. Plotting Cu-MOF response in function of the temperature (Fig. 4b) showed that at all temperatures, the response increased with the concentration of H_2S gas because more gas molecules can be adsorbed onto the sensor surface. The highest response was observed at 150 °C: 5.05, 6.12 and 7.33 in the presence of 1, 5 and 10 ppm H_2S gas, respectively.

At 100 °C, H_2S gas did not have sufficient energy to overcome adsorption barrier on the sensing surface. Also, at 200 °C, the sensor response was decreased relative to 150 °C, it can be surmised that the desorption rate was higher than the adsorption rate, leading to a decrease of the gas response [81].

The net adsorption rate was maximized at the optimal temperature, and consequently, the gas response was increased. Following exposure to 1, 5 and 10 ppm H_2S, CO or NO_2 gas at 150 °C, Cu-MOF resistance diminished in the presence of CO gas (as expected because it is a reducing gas like H_2S gas) and also of NO_2 gas (oxidizing gas) (Fig. 4d). Moreover, the Cu-MOF gas sensor response was higher when exposed to H_2S compared with CO and NO_2 gases at all three tested concentrations (Fig. 4d). For example, the responses to 10 ppm H_2S, CO and NO_2 gases were 7.33, 2.23, and 1.86, respectively.

Then, the dynamic resistance curves of CuO (obtained by calcination at 500 °C) following exposure to 1, 5 and 10 ppm H_2S at different temperatures (250–400 °C) (Fig. 5a and b) indicated that the sensor performed best at 300 °C: 14.25, 16.79, and 20.92 to 1, 5, and 10 ppm H_2S gas, respectively. This also showed that calcination at 500 °C increased the sensing activity of this sensor. In the next step, three CuO gas sensors calcined at different temperatures (400, 500 and 600 °C) were compared. Upon exposure to 1, 5 and 10 ppm H_2S gas at 300 °C (Fig. 5c and d), the best response was observed with the gas sensor calcined at 500 °C. The response to 10 ppm H_2S gas of the sensors

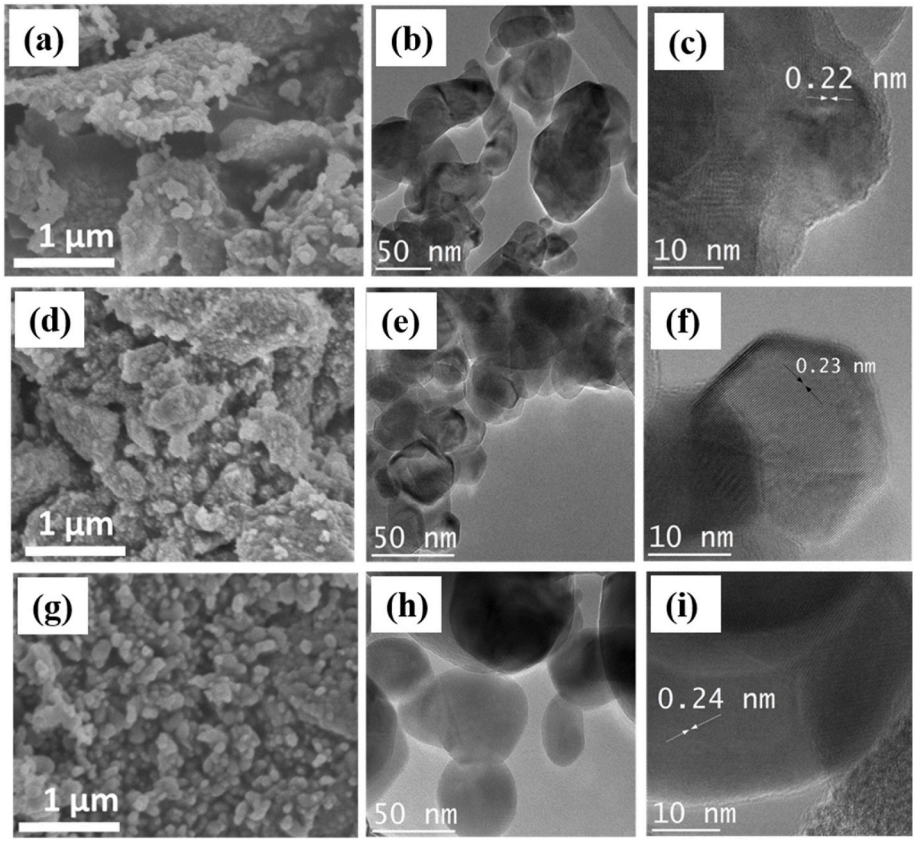

Fig. 2. (a), (d) and (g), SEM (b), (e), (h) TEM and (c), (f), (i) HR-TEM images of MOF-derived CuO (calcined at 500 °C), NiO (calcined at 600 °C) and ZnO (calcined at 600 °C), respectively.

Table 1
Results of the EDS analysis of MOF-derived SMOs.

Sample	Calcination temperature (°C)	Element	Amount (wt %)
MOF-derived CuO	500 °C	Cu	76.9
		O	23.1
MOF-derived NiO	600 °C	Ni	77.3
		O	22.7
MOF-derived ZnO	600 °C	Zn	79.1
		O	20.9

calcined at 400, 500 and 600 °C were 14.09, 20.92 and 12.15, respectively. Lastly, the selectivity of the CuO gas sensor calcined at 500 °C was investigated in the presence of 1, 5 and 10 ppm H_2S, CO, C_6H_6, C_2H_5OH or NO_2 gas at 300 °C (Fig. 6a and b). The responses to 10 ppm H_2S, CO, C_6H_6, C_2H_5OH and NO_2 gases were 20.92, 5.18, 2.93, 2.51 and 2.05, respectively, indicating that this sensor is highly selective towards H_2S gas.

3.2.2. Gas sensors based on Ni-MOF and MOF-derived NiO

Then, the Ni-MOF gas sensor was exposed to 1, 5 and 10 ppm CO gas at 50–200 °C (Fig. 7a). The resistance in the presence of increasing concentrations of CO gas revealed the p-type nature of this gas sensor. In addition, the baseline resistance and resistance variations were limited. Exposure to different concentrations of CO gas and at different temperatures (Fig. 7b) showed that the best responses were obtained at 100 °C: 2.22, 2.47 and 3.02 with 1, 5 and 10 ppm CO gas, respectively. Then, selectivity was evaluated by exposure to increasing concentrations of CO, H_2S, ethanol or NO_2 gases at 100 °C (Fig. 7c and d). This experiment showed that the Ni-MOF gas sensor was more selective for CO gas. For instance, the responses were 3.02, 1.27, 1.39 and 1.33–10 ppm CO, H_2S, ethanol and NO_2 gases, respectively.

Ni-MOF samples calcined at 400, 500 and 600 °C in air for 2 h were used for the next experiments. First, the NiO sensor calcined at 600 °C

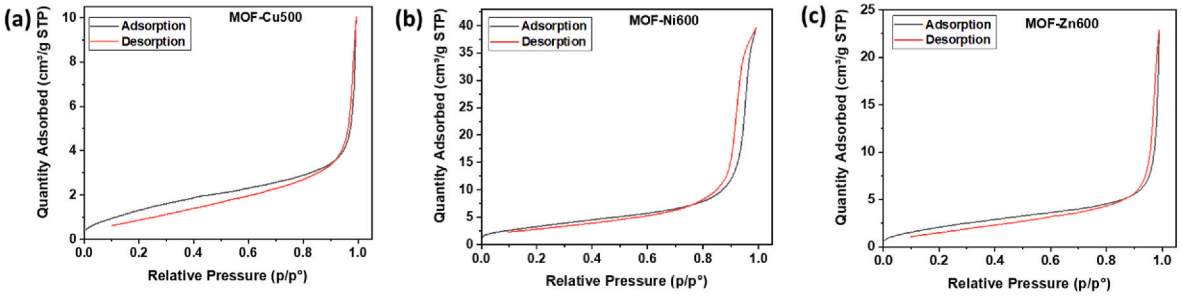

Fig. 3. N_2 adsorption-desorption curves of MOF-derived (a) CuO after calcination at 500 °C, (b) NiO after calcination at 600 °C, and (c) ZnO after calcination at 600 °C.

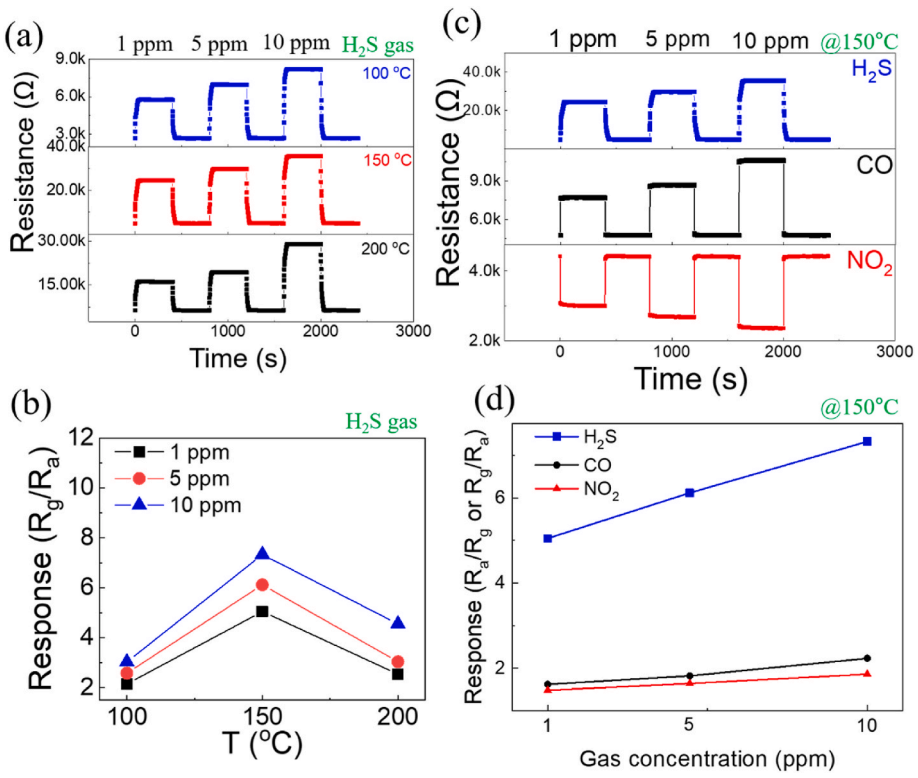

Fig. 4. (a) Cu-MOF gas sensor dynamic resistance curves following exposure to 1, 5 and 10 ppm H_2S gas at 100 °C, 150 °C and 200 °C. (b) Response to different H_2S concentrations in function of the temperature. (c) Cu-MOF gas sensor resistance curves following exposure to 1, 5 and 10 ppm H_2S, CO or NO_2 gas at 150 °C. (d) Response in function of the gas type and its concentration.

was exposed to 1, 5 and 10 ppm CO gas at various temperatures (250–400 °C) (Fig. 8a and b). The sensor displayed a p-type behavior, and the best response was observed at 350 °C: 6.5, 8.66 and 10.49 in the presence of 1, 5 and 10 ppm CO gas, respectively. Comparison of the responses (CO gas at 350 °C) of the three NiO gas sensors calcined at different temperatures (Fig. 8c and d) indicated that the best response was obtained with the sensor calcined at 600 °C. For instance, the responses to 10 ppm CO gas were 4.76, 5.57 and 10.49 for the sensors calcined at 400, 500 and 600 °C, respectively. Lastly, exposure of the NiO sensor calcined at 600 °C to various concentrations of CO, H_2S, H_2, ethanol and NO_2 gases at 350 °C (Fig. 9a and b) highlighted its higher sensitivity towards CO gas. For instance, the responses were 10.49, 1.54, 1.13, 1.11 and 1.22–10 ppm of CO, H_2S, H_2, ethanol and NO_2 gas, respectively.

3.2.3. Gas sensors based on Zn-MOF and MOF-derived ZnO

The Zn-MOF gas sensor was first exposed to 1, 5 and 10 ppm H_2 gas at 50–200 °C (Fig. 10a). The decrease in resistance upon exposure to H_2 gas indicated that the Zn-MOF sensor displayed an n-type behavior. The best responses were obtained at 150 °C (Fig. 10b): 3.45, 4.76 and 5.88 to 1, 5 and 10 ppm H_2 gas, respectively. Exposure to H_2, CO and NO_2 gases at 150 °C (Fig. 10c and d) showed the higher sensitivity of the Zn-MOF gas sensor for H_2 gas (responses to 10 ppm H_2, CO and NO_2 gases: 5.88 and 1.39 and 1.38, respectively).

Calcination of Zn-MOF at 400, 500 and 600 °C was used to obtain ZnO gas sensors. First, the gas sensor calcined at 600 °C was exposed to 1, 5 and 10 ppm H_2 gas at various temperatures (Fig. 11a). The sensor showed an n-type behavior. Then, the response curve of the gas sensor in function of the sensing temperature and H_2 gas concentration (Fig. 11b) indicated that the best response was obtained at 350 °C (10.52, 17.25 and 34.48 to 1, 5 and 10 ppm H_2, respectively). Therefore, calcination significantly increased the response to H_2 gas. Then, comparison of the response of the ZnO sensors calcined at various temperatures to different concentrations (1, 5 and 10 ppm) of H_2 gas at 350 °C (Fig. 11c and d) indicated that calcination at 600 °C gave the best performing gas sensor (Fig. 11d). For instance, the response to 10 ppm H_2 gas were 15.04, 29.23 and 34.48 with the ZnO gas sensors obtained by calcination at 400, 500 and 600 °C, respectively. Lastly, the sensor calcined at 600 °C was exposed to 1, 5 and 10 ppm H_2, CO, ethanol, C_6H_6 and NO_2 gases at 350 °C (Fig. 12a and b). This showed that the ZnO gas sensor was more selective towards H_2 gas. For instance, the responses to 10 ppm H_2, CO, ethanol, C_6H_6 and NO_2 gases were 34.38, 2.37, 1.41, 1.31 and 1.6, respectively.

3.3. Gas sensing mechanism

When resistive gas sensors are exposed to fresh air, the oxygen gas in air with high electron affinity is adsorbed on their surfaces and takes electrons, as described in the following reactions [82]:

$$O_2(g) \rightarrow O_2(ads) \quad (1)$$

$$O_2(ads) + e^- \rightarrow O_2^- \; T < 150\ ^\circ C \quad (2)$$

$$O_2^- + e^- \rightarrow 2O^- \; 150 \leq T < 400\ ^\circ C \quad (3)$$

$$O^- + e^- \rightarrow O^{2-} \; T > 400\ ^\circ C \quad (4)$$

Generally, equation (2) is dominant at low operation temperatures ($T < 150$ °C) and equations (3) and (4) at higher temperatures, namely, $150 \leq T < 400$ °C and $T > 400$ °C, respectively. Depending on their compositions, the gas sensors tested in this study displayed different optimal sensing temperatures (Table 2).

Therefore, the dominant oxygen species were O_2^- for MOF-based sensors because their optimal sensing temperature was 150 °C or lesser, while dominant oxygen species were O^- for MOF-derived SMO-based gas sensors. In the presence of air and electron abstraction by

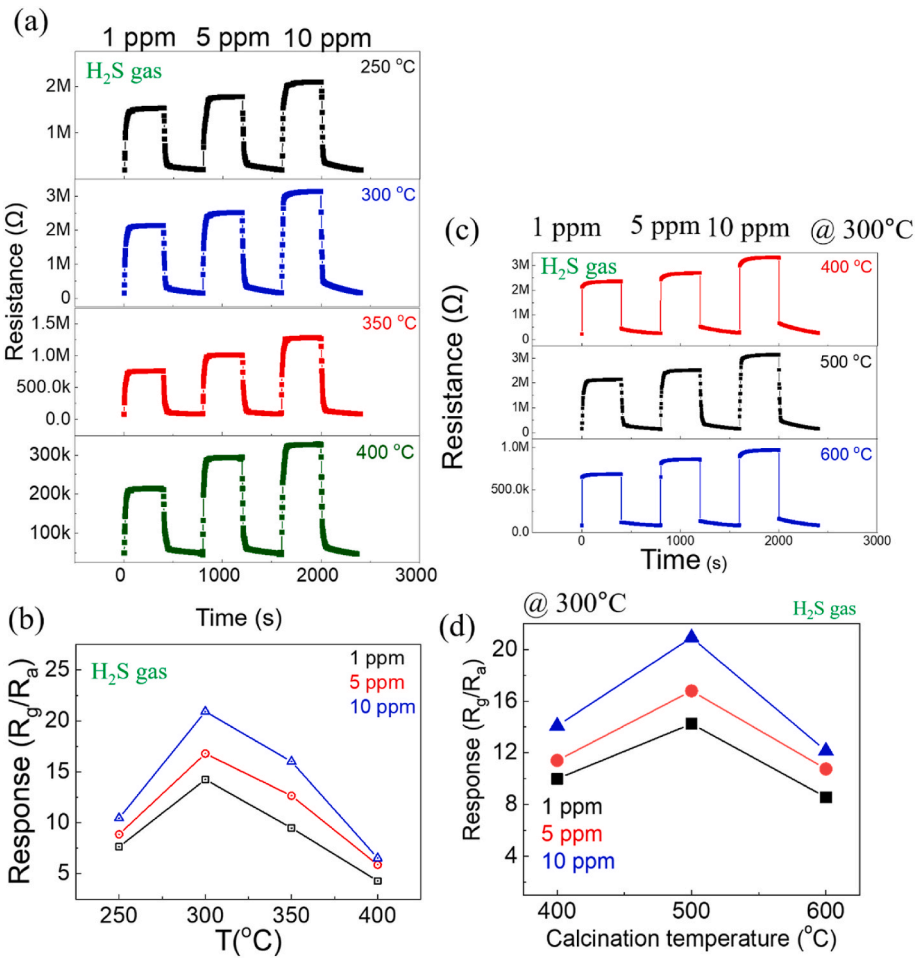

Fig. 5. (a) Dynamic resistance curves of the MOF-derived CuO gas sensor (obtained by calcination at 500 °C) in the presence of 1, 5 and 10 ppm H_2S gas and the indicated temperatures; (b) Response of the gas sensor in function of the sensing temperature and H_2S concentration. (c) Resistance curves and (d) response to 1, 5 and 10 ppm H_2S gas at 300 °C of CuO gas sensors obtained by calcination at 400, 500 or 600 °C.

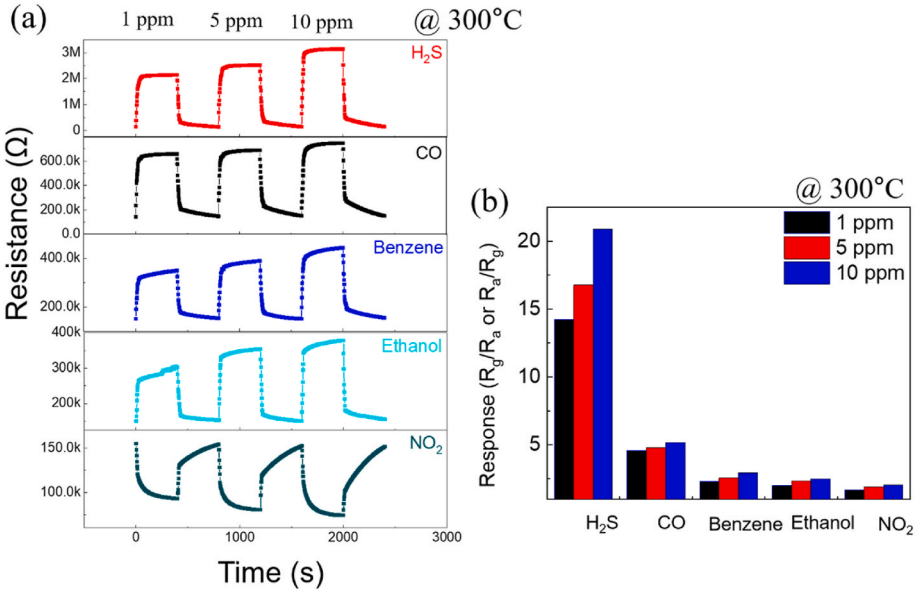

Fig. 6. (a) Dynamic Resistance curves of the MOF-derived CuO sensor (obtained by calcination at 500 °C) in the presence of 1, 5 and 10 ppm of the indicated gases at 300 °C. (b) Corresponding selectivity graph.

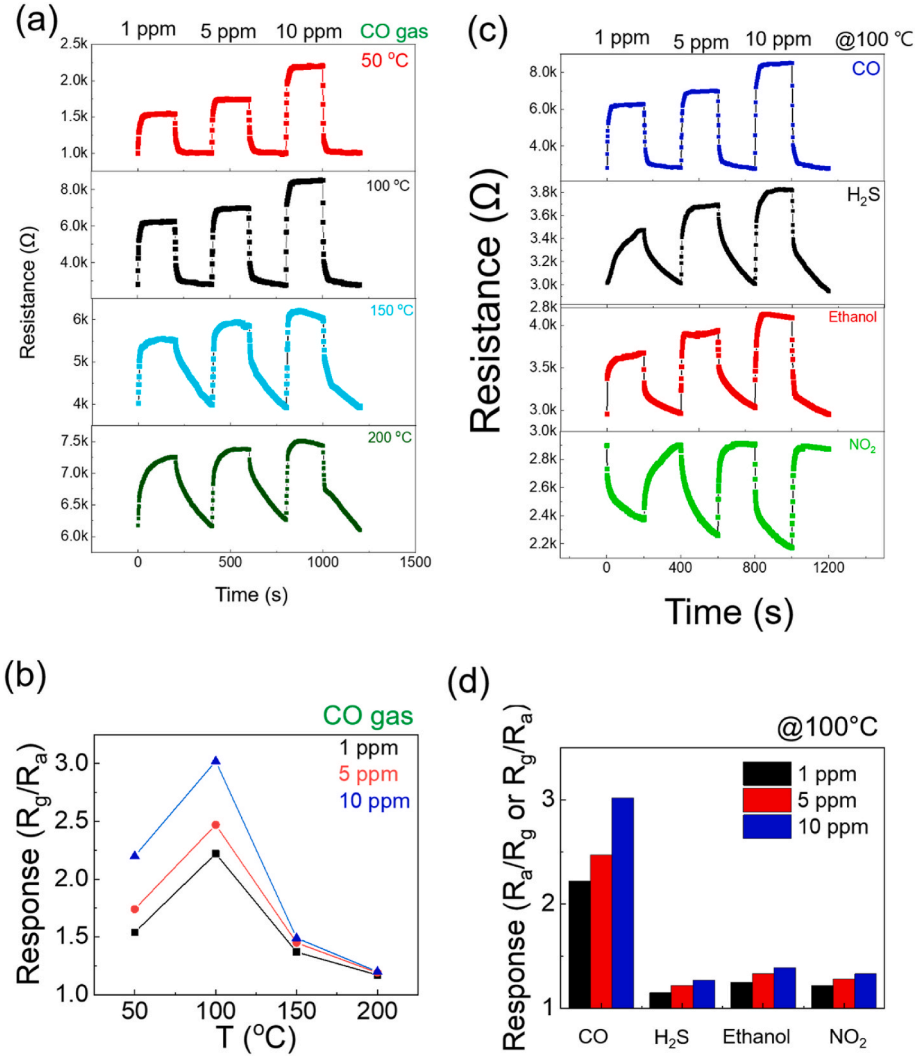

Fig. 7. (a) Dynamic resistance curves of the Ni-MOF gas sensor in the presence of 1, 5 and 10 ppm CO gas at the indicated temperatures. (b) Response curves in function of the temperature and CO gas concentration. (c) Dynamic resistance of the Ni-MOF gas sensor in the presence of 1, 5 and 10 ppm of CO, H_2S, ethanol and NO_2 gases at 100 °C. (d) Corresponding selectivity graphs.

oxygen ions, an electron depletion layer is formed on the surface of n-type sensors (Table 2), in which the amount of electrons is lower than that in the core regions, and accordingly, the sensor resistance is higher compared with the vacuum condition [83]. For p-type gas sensors (Table 2), as a result of the abstract of electrons, a hole accumulation layer is formed on the sensor surface, resulting in the formation of a hole-rich layer that ultimately leads to lower resistance in air compared with the vacuum condition [84]. Upon exposure to reducing gases such as CO, H_2S and H_2, the following reactions are expected [85]:

$$CO + O^- \rightarrow CO_2 + e \; T = 100\ ^\circ C \quad (5)$$

$$2CO + O_2^- \rightarrow 2CO_2 + e \; T = 350\ ^\circ C \quad (6)$$

$$2H_2 + O_2^- \rightarrow 2H_2O + e \; T = 150\ ^\circ C \quad (7)$$

$$H_2 + O^- \rightarrow H_2O + e \; T = 350\ ^\circ C \quad (8)$$

$$2H_2S + 3O_2^- \rightarrow 2SO_2 + 2H_2O + 3e \; T = 150\ ^\circ C \quad (9)$$

$$H_2S + 3O^- \rightarrow SO_2 + H_2O + 3e \; T = 300\ ^\circ C \quad (10)$$

Although MOF-based sensors had a larger surface area compared with SMO-derived gas sensors, their sensing performance was weaker, possibly due to the lower charge carrier mobility. Also, as all tested MOF-based gas sensors had low baseline resistance values in air (<20 kΩ), no significant resistance variation was occurred in the presence of target gases, resulting in a low response. In addition, the non-covalent interactions gases occurring on the surface of MOF-based gas sensors (*i.e.* van der Waals forces, hydrogen bonding, and π-π interactions) led to minimal electrical resistance change [86] In SMO-based gas sensors, the higher charge carrier mobility and baseline resistance values led to larger resistance variations upon exposure to gases and consequently higher responses were observed.

Each SMO-based sensor exhibited selectivity towards a specific gas (Table 2). The high selectivity towards H_2S gas observed for the MOF-derived CuO sensor can be mainly related to conversion of CuO to CuS in the presence of H_2S, as follows [87].

$$CuO + H_2S \rightarrow CuS + H_2O\ (g) \quad (11)$$

According to the above reaction, H_2S can directly react with semiconducting CuO and convert it to CuS with high metallic-like conductivity. Previously, the formation of CuS upon exposure of CuO to H_2S gas has been demonstrated by theoretical models or experimental evidence [88–91]. Therefore, in the presence of H_2S gas, the electrical resistance significantly changes, explaining the higher selectivity towards this gas. It should be noted that equation (9) is valid when other SMOs, such as NiO, are exposed to H_2S gas; however, for CuO, the main reaction can be assumed to be the one described in equations (9) and (10).

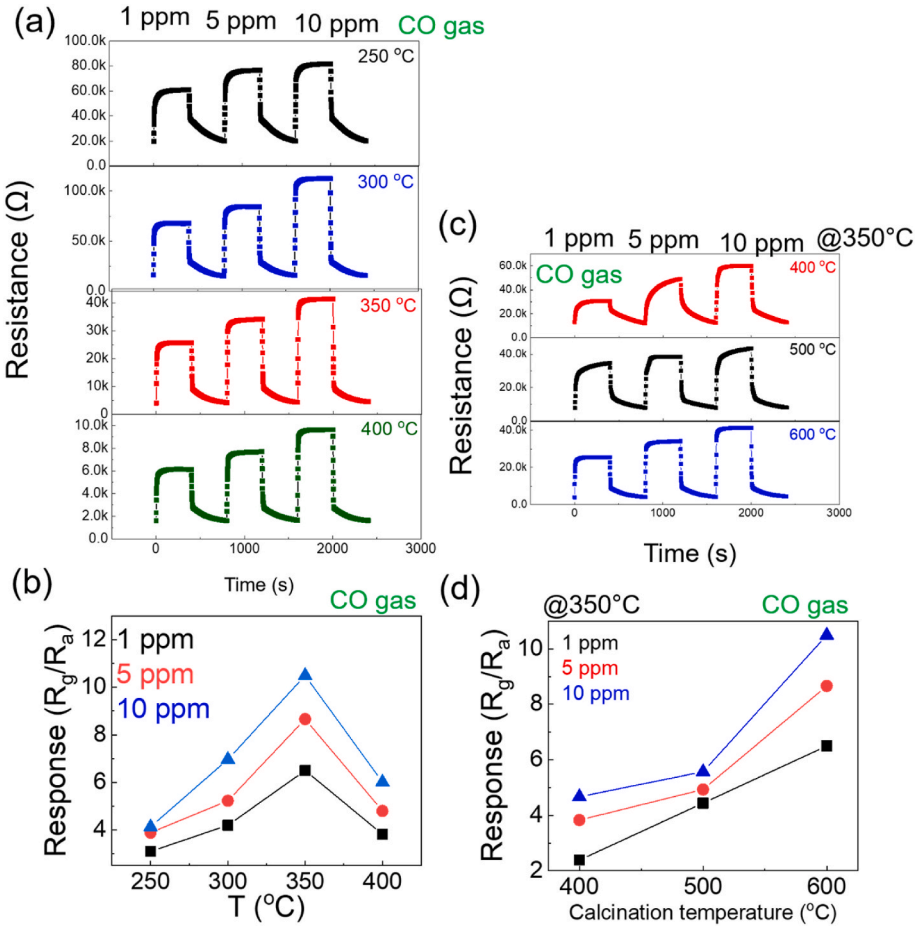

Fig. 8. Resistance changes of the NiO gas sensor calcined at 600 °C to 1, 5 and 10 ppm CO gas at 250, 300, 350 and 400 °C. (b) Response curves in function of the sensing temperature and CO concentration. (c) Resistance curves and (d) response of the NiO gas sensors in function of the calcination temperature and CO gas concentration at 350 °C.

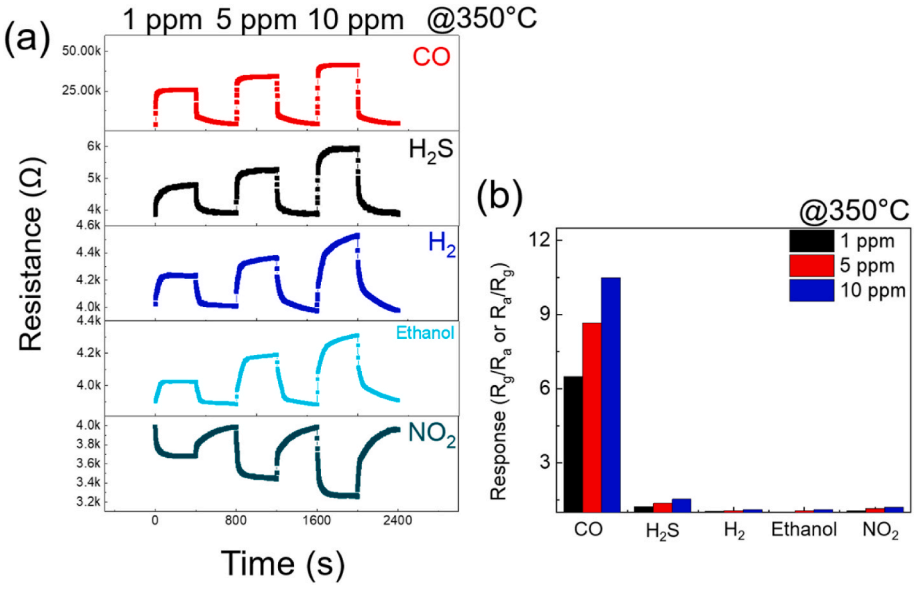

Fig. 9. (a) Resistance curves of the MOF-derived NiO sensor obtained by calcination at 600 °C to the indicated gases at 350 °C. (b) Corresponding selectivity graph.

The MOF-derived ZnO sensor displayed high selectivity towards H_2 gas that can be related to the highly reducing nature of H_2 gas and the formation of metallic Zn with higher conductivity compared with Zn on the surface of ZnO at the sensing temperature [92].

$$ZnO + H_2 \rightarrow Zn(s) + H_2O(g) \quad (12)$$

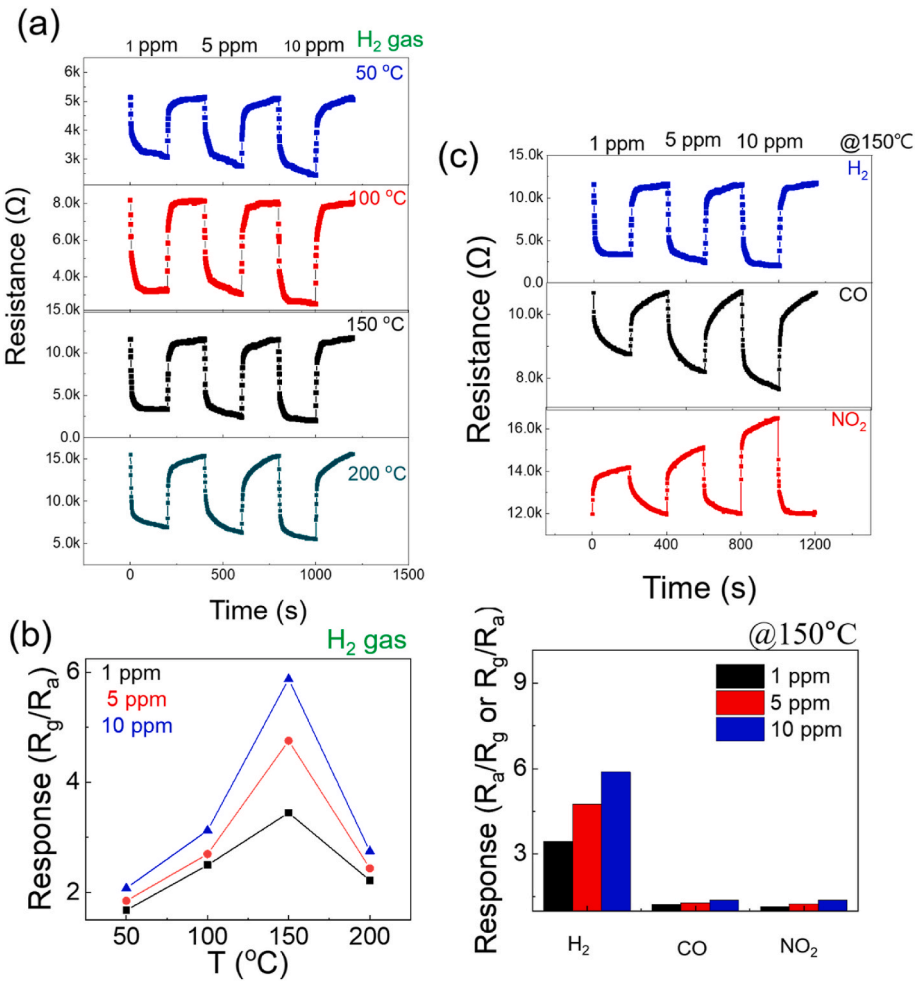

Fig. 10. (a) Resistance curves of the Zn-MOF gas sensor upon exposure to 1, 5 and 10 ppm H_2 gas at the indicated temperatures. (b) Response curve in function of H_2 gas concentration and temperature. (c) Resistance curves of the Zn-MOF gas sensor to the indicated gases at 150 °C. (d) Corresponding selectivity graphs.

This explains the higher selectivity towards H_2 gas compared with other gases.

Also, the MOF-derived NiO sensor was more selective towards CO gas, mainly due to the good catalytic activity of NiO towards CO gas [93] and easy oxidation of CO to CO_2 gas on NiO surface at the sensing temperature.

Although some surface residual carbons were detected by XPS, their effects on the sensing mechanism were not significant because they did not form a major phase in the XRD profiles. However, the oxygen species attached to residual carbons could participate in the sensing reactions.

Table 3 compares the H_2S, H_2, and CO gas sensing properties of the present work with those reported in the literature. Overall, it can be seen that the response values obtained in the present study are comparable and even, in most cases better than those reported in the literature.

4. Conclusions

M-MOFs (M = Cu, Ni and Zn) and MOF-derived CuO, NiO and ZnO SMOs were synthesized for gas sensing studies. The morphological and structural analyses confirmed the synthesis of metal oxides with the desired morphology, chemical composition and phases. The gas sensing studies revealed the better performance of the MOF-derived metal oxides compared with their MOF templates, but at higher optimal sensing temperatures. Moreover, the MOF-derived metal oxide sensing performance was influenced by their calcination temperature. Indeed, the best selectivity towards H_2S, CO and H_2 gases were obtained with CuO, NiO and ZnO gas sensors calcined at 500, 600 and 600 °C, respectively. This research represents a significant advancement in the field of gas sensor technology, offering innovative MOF-derived metal oxide sensors with tailored properties for precise and reliable gas detection in various industrial and environmental settings. Future studies should investigate the fabrication of sensor arrays to easily detect the different gases present in a gas mixture.

CRediT authorship contribution statement

Carmen Montoro: Writing – original draft, Validation, Investigation, Formal analysis, Data curation, Conceptualization. **Jin-Young Kim:** Writing – original draft, Methodology, Investigation, Formal analysis, Data curation. **Ali Mirzaei:** Writing – original draft, Validation, Methodology, Investigation, Formal analysis, Data curation, Conceptualization. **Jae-Hyoung Lee:** Writing – review & editing, Validation, Methodology, Investigation, Formal analysis, Data curation, Conceptualization. **Syreina Sayegh:** Writing – review & editing, Validation, Methodology, Formal analysis, Data curation. **Elissa Makhoul:** Writing – review & editing, Validation, Methodology, Investigation, Formal analysis, Data curation. **Igor Iatsunskyi:** Writing – review & editing, Validation, Methodology, Investigation, Formal analysis, Data curation. **Emerson Coy:** Writing – review & editing, Validation, Methodology, Investigation, Formal analysis, Data curation. **Mikhael Bechelany:** Writing – review & editing, Validation, Supervision, Resources, Project administration, Methodology, Funding acquisition, Conceptualization. **Hyoun Woo Kim:** Writing – review & editing, Validation, Supervision, Resources, Funding acquisition, Conceptualization. **Sang Sub Kim:**

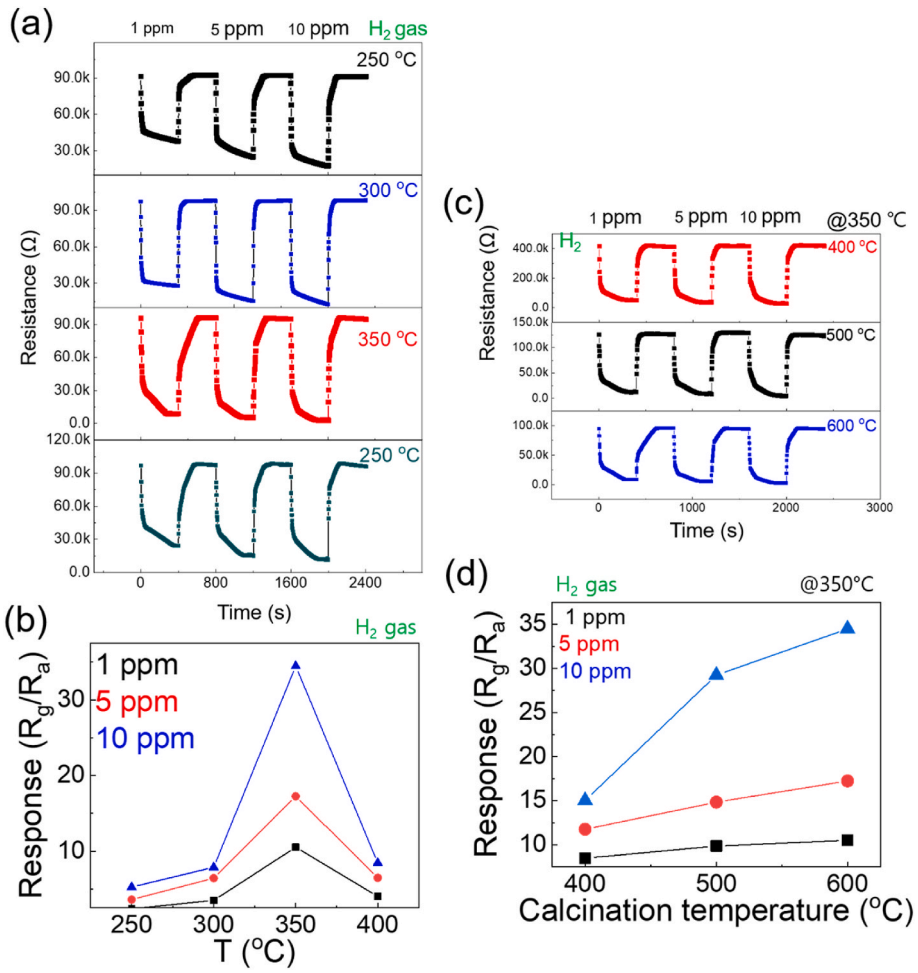

Fig. 11. Resistance changes of the MOF-derived ZnO gas sensor obtained by calcination at 600 °C to 1, 5 and 10 ppm H_2 gas at the indicated sensing temperatures. (b) Response curve in function of the sensing temperature and H_2 concentration. (c) Resistance curves and (d) Response of the ZnO gas sensors obtained by calcination at 400, 500 and 600 °C to 1, 5 and 10 ppm H_2 gas at 350 °C.

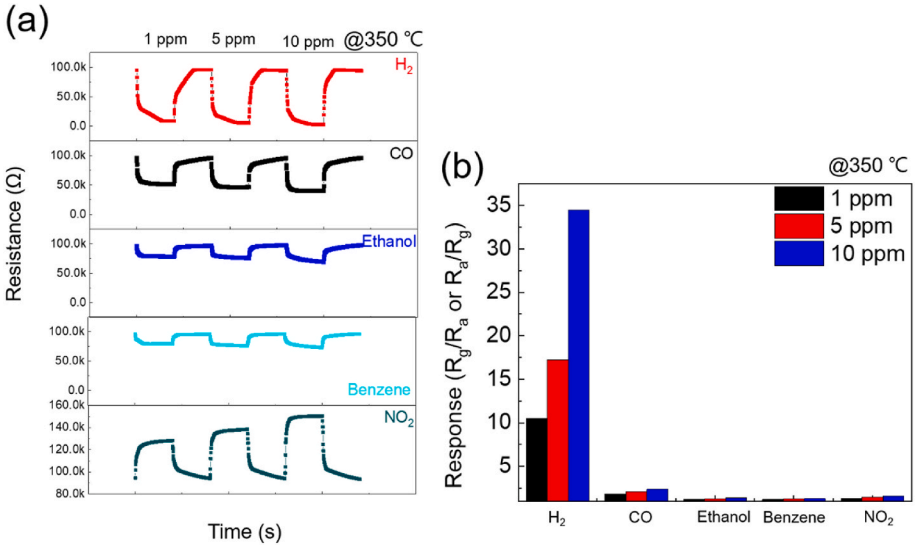

Fig. 12. (a) Resistance curves of the MOF-derived ZnO sensor obtained by calcination at 600 °C to 1, 5 and 10 ppm H_2, CO, ethanol, C_6H_6 and NO_2 gas at 350 °C. (b) Corresponding selectivity graph.

Table 2
Optimal sensing temperature, selectivity and conductivity type of the different gas sensors tested in this study.

Sensor	Optimal temperature (°C)	Selectivity	Conductivity
Cu-MOF	150	H_2S gas (low selectivity)	p-type
MOF-derived CuO calcined at 500 °C	300	H_2S gas (high selectivity)	
Ni-MOF	100	CO gas (low selectivity)	
MOF-derived NiO calcined at 600 °C	350	CO gas (high selectivity)	
Zn-MOF	150	H_2 gas (low selectivity)	n-type
MOF-derived ZnO calcined at 600 °C	350	H_2 gas (high selectivity)	

Table 3
Comparison of H_2S, H_2 and CO gas sensing properties of present work with those reported in the literature.

Material	Gas and conc. (ppm)	T (°C)	Response (R_a/R_g) or (R_g/R_a)	Ref.
MOF-derived CuO calcined at 500 °C	**H_2S (10)**	**300**	**20.92**	**This work**
MOF-derived ZnO–CuO composite	H_2S (10)	350	~12	[94]
MOF-derived Ru-doped Fe_2O_3 hollow nanobox	H_2S (10)	200	~11	[95]
MOF-derived $CuFe_2O_4$ NPs	H_2S (50)	210	210	[96]
MOF-derived Co_3O_4/$NiCo_2O_4$	H_2S (50)	~6	225	[97]
MOF-derived Co_3O_4/ZnO	H_2S (10)	5	250	[98]
MOF-derived ZnO calcined at 600 °C	**H_2 (10)**	**350**	**34.48**	**This work**
MOF-derived WO_3–C/In_2O_3 heterostructures	H_2 (200)	250	4.19	[99]
Au-decorated ZnO	H_2 (100)	230	37.6	[100]
Pt-decorated ZnO	H_2 (15)	250	~6 (I_g/I_a)	[101]
Ag-decorated ZnO	H_2 (300)	250	~5	[102]
ZnO nanorod arrays	H_2 (2000)	225	~25	[103]
MOF-derived NiO calcined at 600 °C	**CO (10 ppm)**	**350**	**10.49**	**This work**
MOF-derived NiO/SnO_2	CO (10 ppm)	25	2.5	[104]
MOF-derived porous In_2O_3/Fe_2O_3 core–shell nanotubes	CO (200 ppm)	260	33.7	[105]
MOF-derived SnO_2/$MoSe_2$ composite	CO (200 ppm)	25	10 % [(R_a−R_g)/R_a × 100 %]	[106]
Co_3O_4@TiO_2 nanocomposite	CO (100 ppm)	140	16	[107]
CuO/TiO_2 heterojunction	CO (800 ppm)	250	~9	[108]

Writing – review & editing, Validation, Supervision, Resources, Methodology, Funding acquisition, Conceptualization.

Declaration of Competing interest

We declare no interest.

Data availability

Data will be made available on request.

Acknowledgements

This research was supported by the Nano & Material Technology Development Program through the National Research Foundation of Korea(NRF) funded by the Ministry of Science and ICT(RS-2024-00412249).

Appendix A. Supplementary data

Supplementary data to this article can be found online at https://doi.org/10.1016/j.compositesb.2024.111637.

References

[1] Karuppasamy K, Sharma A, Vikraman D, Lee YA, Sivakumar P, Korvink JG, et al. Room-temperature response of MOF-derived Pd@PdO core shell/γ-Fe2O3 microcubes decorated graphitic carbon based ultrasensitive and highly selective H2 gas sensor. J Colloid Interface Sci 2023;652:692–704. https://doi.org/10.1016/j.jcis.2023.07.046.
[2] Luo Y, An B, Bai J, Wang Y, Cheng X, Wang Q, et al. Ultrahigh-response hydrogen sensor based on PdO/NiO co-doped In2O3 nanotubes. J Colloid Interface Sci 2021;599:533–42. https://doi.org/10.1016/j.jcis.2021.04.125.
[3] Pham TKN, Brown JJ. Hydrogen sensors using 2-dimensional materials: a review. ChemistrySelect 2020;5:7277–97. https://doi.org/10.1002/slct.202000788.
[4] Duc Chinh N, Haneul Y, Minh Hieu N, Manh Hung N, Duc Quang N, Kim C, et al. pn-Heterojunction of the SWCNT/ZnO nanocomposite for temperature dependent reaction with hydrogen. J Colloid Interface Sci 2021;584:582–91. https://doi.org/10.1016/j.jcis.2020.10.017.
[5] Hübert T, Boon-Brett L, Black G, Banach U. Hydrogen sensors - a review. Sens Actuators B Chem 2011;157:329–52. https://doi.org/10.1016/j.snb.2011.04.070.
[6] Zhu S, Tian Q, Wu G, Bian W, Sun N, Wang X, et al. Highly sensitive and stable H2 gas sensor based on p-PdO-n-WO3-heterostructure-homogeneously-dispersing thin film. Int J Hydrogen Energy 2022;47:17821–34. https://doi.org/10.1016/j.ijhydene.2022.03.237.
[7] Drmosh QA, Yamani ZH, Hendi AH, Gondal MA, Moqbel RA, Saleh TA, et al. A novel approach to fabricating a ternary rGO/ZnO/Pt system for high-performance hydrogen sensor at low operating temperatures. Appl Surf Sci 2019;464:616–26. https://doi.org/10.1016/j.apsusc.2018.09.128.
[8] Darmadi I, Nugroho FAA, Langhammer C. High-performance nanostructured palladium-based hydrogen sensors - current limitations and strategies for their mitigation. ACS Sens 2020;5:3306–27. https://doi.org/10.1021/acssensors.0c02019.
[9] Mirzaei A, Kim SS, Kim HW. Resistance-based H2S gas sensors using metal oxide nanostructures: a review of recent advances. J Hazard Mater 2018;357:314–31. https://doi.org/10.1016/j.jhazmat.2018.06.015.
[10] Georgiadis AG, Charisiou ND, Goula MA. Removal of hydrogen sulfide from various industrial gases: a review of the most promising adsorbing materials. Catalysts 2020;10. https://doi.org/10.3390/catal10050521.
[11] Yang S, Sun J, Xu L, Zhou Q, Chen X, Zhu S, et al. Au@ZnO functionalized three–dimensional macroporous WO3: a application of selective H2S gas sensor for exhaled breath biomarker detection. Sens Actuators B Chem 2020;324. https://doi.org/10.1016/j.snb.2020.128725.
[12] Mahajan S, Jagtap S. Metal-oxide semiconductors for carbon monoxide (CO) gas sensing: a review. Appl Mater Today 2020;18:100483. https://doi.org/10.1016/j.apmt.2019.100483.
[13] Omaye ST. Metabolic modulation of carbon monoxide toxicity. n.d.
[14] Kinoshita H, Türkan H, Vucinic S, Naqvi S, Bedair R, Rezaee R, et al. Carbon monoxide poisoning. Toxicol Rep 2020;7:169–73. https://doi.org/10.1016/j.toxrep.2020.01.005.
[15] Lv S, Zhang K, Zhu L, Tang D, Niessner R, Knopp D. H2-Based electrochemical biosensor with Pd Nanowires@ZIF-67 molecular sieve bilayered sensing interface for immunoassay. Anal Chem 2019;91:12055–62. https://doi.org/10.1021/acs.analchem.9b03177.
[16] Del Orbe Henriquez D, Cho I, Yang H, Choi J, Kang M, Chang KS, et al. Pt nanostructures fabricated by local hydrothermal synthesis for low-power catalytic-combustion hydrogen sensors. ACS Appl Nano Mater 2021;4:7–12. https://doi.org/10.1021/acsanm.0c02794.
[17] Hamagami J, Oh Y, Watanabe Y, Takata M. Preparation and characterization of an optically detectable H2 gas sensor consisting of Pd/MoO3 thin films. Sens Actuators B Chem 1993;13:281–3. https://doi.org/10.1016/0925-4005(93)85381-J.
[18] Constantinoiu I, Viespe C. Development of Pd/TiO2 porous layers by pulsed laser deposition for surface acoustic wave H2 gas sensor. Nanomaterials 2020;10:760–70. https://doi.org/10.3390/nano10040760.
[19] Yoon JH, Kim BJ, Kim JS. Design and fabrication of micro hydrogen gas sensors using palladium thin film. Mater Chem Phys 2012;133:987–91. https://doi.org/10.1016/j.matchemphys.2012.02.002.
[20] Mirzaei A, Kim JH, Kim HW, Kim SS. Gasochromic WO3 nanostructures for the detection of hydrogen gas: an overview. Appl Sci 2019;9. https://doi.org/10.3390/app9091775.
[21] Mirzaei A, Yousefi HR, Falsafi F, Bonyani M, Lee JH, Kim JH, et al. An overview on how Pd on resistive-based nanomaterial gas sensors can enhance response toward hydrogen gas. Int J Hydrogen Energy 2019;44:20552–71. https://doi.org/10.1016/j.ijhydene.2019.05.180.

[22] Paliwal A, Sharma A, Tomar M, Gupta V. Carbon monoxide (CO) optical gas sensor based on ZnO thin films. Sens Actuators B Chem 2017;250:679–85. https://doi.org/10.1016/j.snb.2017.05.064.

[23] Vargas AP, Gámez F, Roales J, Lopes-Costa T, Pedrosa JM. A paper-based ultrasensitive optical sensor for the selective detection of H2 S vapors. Chemosensors 2021;9:1–14. https://doi.org/10.3390/chemosensors9020040.

[24] Hyodo T, Ishibashi C, Matsuo K, Kaneyasu K, Yanagi H, Shimizu Y. CO and CO2 sensing properties of electrochemical gas sensors using an anion-conducting polymer as an electrolyte. Electrochim Acta 2012;82:19–25. https://doi.org/10.1016/j.electacta.2012.03.142.

[25] Khan MA, Qazi F, Hussain Z, Idrees MU, Soomro S, Soomro S. Recent trends in electrochemical detection of NH3, H2S and NOx gases. Int J Electrochem Sci 2017;12:1711–33. https://doi.org/10.20964/2017.03.76.

[26] Luo W, Fu Q, Zhou D, Deng J, Liu H, Yan G. A surface acoustic wave H2S gas sensor employing nanocrystalline SnO2 thin film. Sens Actuators B Chem 2013;176:746–52. https://doi.org/10.1016/j.snb.2012.10.086.

[27] Nagai D, Nakashima T, Nishibori M, Itoh T, Izu N, Shin W. Thermoelectric gas sensor with CO combustion catalyst for ppm level carbon monoxide detection. Sens Actuators B Chem 2013;182:789–94. https://doi.org/10.1016/j.snb.2013.03.061.

[28] Kim JH, Mirzaei A, Kim HW, Kim SS. Improving the hydrogen sensing properties of SnO2 nanowire-based conductometric sensors by Pd-decoration. Sens Actuators B Chem 2019;285:358–67. https://doi.org/10.1016/j.snb.2019.01.008.

[29] Nanofiber PIOZ, Kim SS. Ppb-level selective hydrogen gas detection of. Sensors 2019;19:4276–88. https://doi.org/10.3390/s19194276.

[30] Kim JH, Mirzaei A, Kim HW, Kim SS. Pd functionalization on ZnO nanowires for enhanced sensitivity and selectivity to hydrogen gas. Sens Actuators B Chem 2019;297:126693. https://doi.org/10.1016/j.snb.2019.126693.

[31] Li C, Choi PG, Kim K, Masuda Y. High performance acetone gas sensor based on ultrathin porous NiO nanosheet. Sens Actuators B Chem 2022;367:132143. https://doi.org/10.1016/j.snb.2022.132143.

[32] Güldüren ME, İskenderoğlu D, Güney H, Morkoç Karadeniz S, Acar M, Gür E. Structural, optical, and H2 gas sensing analyses of Cr doped CuO thin films grown by ultrasonic spray pyrolysis. Int J Hydrogen Energy 2023;8:20804–14. https://doi.org/10.1016/j.ijhydene.2023.03.057.

[33] Lee H-S, Kim J, Moon H, Lee W. Hydrogen gas sensors using palladium nanogaps on an elastomeric substrate. Adv Mater 2021;33:2005929. https://doi.org/10.1002/adma.202005929.

[34] Wang S, McGuirk CM, D'Aquino A, Mason JA, Mirkin CA. Metal–organic framework nanoparticles. Adv Mater 2018;30:1800202–16. https://doi.org/10.1002/adma.201800202.

[35] Jiang Y, Hu Y, Luan B, Wang L, Krishna R, Ni H, et al. Benchmark single-step ethylene purification from ternary mixtures by a customized fluorinated anion-embedded MOF. Nat Commun 2023;14:401–10. https://doi.org/10.1038/s41467-023-35984-5.

[36] Huang J, Xu Z, Jiang Y, Law W cheung, Dong B, Zeng X, et al. Metal organic framework-coated gold nanorod as an on-demand drug delivery platform for chemo-photothermal cancer therapy. J Nanobiotechnology 2021;19:219–32. https://doi.org/10.1186/s12951-021-00961-x.

[37] Hu Z, Deibert BJ, Li J. Luminescent metal-organic frameworks for chemical sensing and explosive detection. Chem Soc Rev 2014;43:5815–40. https://doi.org/10.1039/c4cs00010b.

[38] Grape ES, Chacón-garcía AJ, Rojas S, Pérez Y, Jaworski A, Nero M, et al. Removal of pharmaceutical pollutants from effluent by a plant-based metal – organic framework. Nature water 2023;1:433–42. https://doi.org/10.1038/s44221-023-00070-z.

[39] Pascanu V, González Miera G, Inge AK, Martín-Matute B. Metal-organic frameworks as catalysts for organic synthesis: a critical perspective. J Am Chem Soc 2019;141:7223–34. https://doi.org/10.1021/jacs.9b00733.

[40] Zhou J, Wang B. Emerging crystalline porous materials as a multifunctional platform for electrochemical energy storage. Chem Soc Rev 2017;46:6927–45. https://doi.org/10.1039/c7cs00283a.

[41] Yap MH, Fow KL, Chen GZ. Synthesis and applications of MOF-derived porous nanostructures. Green Energy Environ 2017;2:218–45. https://doi.org/10.1016/j.gee.2017.05.003.

[42] Qiu T, Liang Z, Guo W, Tabassum H, Gao S, Zou R. Metal–organic framework-based materials for energy conversion and storage. ACS Energy Lett 2020;5:520–32. https://doi.org/10.1021/acsenergylett.9b02625.

[43] Farid S, Ren S, Hao C. MOF-derived metal/carbon materials as oxygen evolution reaction catalysts. Inorg Chem Commun 2018;94:57–74. https://doi.org/10.1016/j.inoche.2018.06.008.

[44] Wang G, Yang S, Cao L, Jin P, Zeng X, Zhang X, et al. Engineering mesoporous semiconducting metal oxides from metal-organic frameworks for gas sensing. Coord Chem Rev 2021;445:214086. https://doi.org/10.1016/j.ccr.2021.214086.

[45] Gonçalves JM, Martins PR, Rocha DP, Matias TA, Julião MSS, Munoz RAA, et al. Recent trends and perspectives in electrochemical sensors based on MOF-derived materials. J Mater Chem C Mater 2021;9:8718–45. https://doi.org/10.1039/d1tc02025k.

[46] Yao MS, Li WH, Xu G. Metal–organic frameworks and their derivatives for electrically-transduced gas sensors. Coord Chem Rev 2021;426:213479. https://doi.org/10.1016/j.ccr.2020.213479.

[47] Koo W-T, Jang J-S, Kim I-D. Metal-organic frameworks for chemiresistive sensors. Chem 2019;5:1938–63. https://doi.org/10.1016/j.chempr.2019.04.013.

[48] Zhang S, Ding Y, Wang Q, Song P. MOFs-derived In2O3/ZnO/Ti3C2TX MXene ternary nanocomposites for ethanol gas sensing at room temperature. Sens Actuators B Chem 2023;393:134122. https://doi.org/10.1016/j.snb.2023.134122.

[49] Liu M, Wang J, Song P, Ji J, Wang Q. Metal-organic frameworks-derived In2O3 microtubes/Ti3C2Tx MXene composites for NH3 detection at room temperature. Sens Actuators B Chem 2022;361:131755. https://doi.org/10.1016/j.snb.2022.131755.

[50] Wei H, Zhang H, Song B, Yuan K, Xiao H, Cao Y, et al. Metal–organic framework (MOF) derivatives as promising chemiresistive gas sensing materials: a review. Int J Environ Res Public Health 2023;20. https://doi.org/10.3390/ijerph20054388.

[51] Nguyen DK, Lee JH, Doan TLH, Nguyen TB, Park S, Kim SS, et al. H2 gas sensing of Co-incorporated metal-organic frameworks. Appl Surf Sci 2020;523:146487. https://doi.org/10.1016/j.apsusc.2020.146487.

[52] Nguyen D-K, Lee J-H, Nguyen T-B, Le Hoang Doan T, Phan BT, Mirzaei A, et al. Realization of selective CO detection by Ni-incorporated metal-organic frameworks. Sens Actuators B Chem 2020;315:128110. https://doi.org/10.1016/j.snb.2020.128110.

[53] Aykanat A, Meng Z, Stolz RM, Morrell CT, Mirica KA. Bimetallic two-dimensional metal–organic frameworks for the chemiresistive detection of carbon monoxide. Angew Chem Int Ed 2022;61:e202113665. https://doi.org/10.1002/anie.202113665.

[54] Surya SG, Bhanoth S, Majhi SM, More YD, Teja VM, Chappanda KN. A silver nanoparticle-anchored UiO-66(Zr) metal–organic framework (MOF)-based capacitive H2S gas sensor. CrystEngComm 2019;21:7303–12. https://doi.org/10.1039/C9CE01323G.

[55] Drobek M, Kim JH, Bechelany M, Vallicari C, Julbe A, Kim SS. MOF-based membrane encapsulated ZnO nanowires for enhanced gas sensor selectivity. ACS Appl Mater Interfaces 2016;8:8323–8. https://doi.org/10.1021/acsami.5b12062.

[56] Weber M, Kim JH, Lee JH, Kim JY, Iatsunskyi I, Coy E, et al. High-performance nanowire hydrogen sensors by exploiting the synergistic effect of Pd nanoparticles and metal-organic framework membranes. ACS Appl Mater Interfaces 2018;10:34765–73. https://doi.org/10.1021/acsami.8b12569.

[57] Li Y, Xu Y, Yang W, Shen W, Xue H, Pang H. MOF-derived metal oxide composites for advanced electrochemical energy storage. Small 2018;14:1704435. https://doi.org/10.1002/smll.201704435.

[58] Wu S, Liu J, Wang H, Yan H. A review of performance optimization of MOF-derived metal oxide as electrode materials for supercapacitors. Int J Energy Res 2019;43:697–716. https://doi.org/10.1002/er.4232.

[59] Yi S, Shi W, Yang X, Yao Z. Engineering sensitive gas sensor based on MOF-derived hollow metal-oxide semiconductor heterostructures. Talanta 2023;258:124442. https://doi.org/10.1016/j.talanta.2023.124442.

[60] Dmello ME, Vishwanathan S, Bakuru VR, Shanbhag GV, Kalidindi SB. Metal-organic framework-derived Co-doped ZnO nanostructures anchored on N-doped carbon as a room-temperature chemiresistive hydrogen sensor. ACS Appl Nano Mater 2023;6:238–47. https://doi.org/10.1021/acsanm.2c04256.

[61] Hussain S, Okai Amu-Darko JN, Wang M, Alothman AA, Ouladsmane M, Aldossari SA, et al. CuO-decorated MOF derived ZnO polyhedral nanostructures for exceptional H2S gas detection. Chemosphere 2023;317. https://doi.org/10.1016/j.chemosphere.2023.137827.

[62] Chen M, Li X, Li Y, Li Y, Qin Z, Wang Q. MOF-derived Co3O4 nanoparticles over direct grown ZnO nanoflower on ceramic for CO sensor with high selectivity. Sens Actuators B Chem 2024;401:134951. https://doi.org/10.1016/j.snb.2023.134951.

[63] Procopio EQ, Linares F, Montoro C, Colombo V, Maspero A, Barea E, et al. Cation-exchange porosity tuning in anionic metal-organic frameworks for the selective separation of gases and vapors and for catalysis. Angew Chem Int Ed 2010;49:7308–19. https://doi.org/10.1002/anie.201003314.

[64] Padial NM, Quartapelle Procopio E, Montoro C, López E, Oltra JE, Colombo V, et al. Highly hydrophobic isoreticular porous metal-organic frameworks for the capture of harmful volatile organic compounds. Angew Chem Int Ed 2013;52:8290–4. https://doi.org/10.1002/anie.201303484.

[65] Dybtsev DN, Chun H, Kim K. Rigid and flexible: a highly porous metal-organic framework with unusual guest-dependent dynamic behavior. Angew Chem Int Ed 2004;43:5033–6. https://doi.org/10.1002/anie.200460712.

[66] Bala N, Singh HK, Verma S, Rath S. Magnetic-order induced effects in nanocrystalline NiO probed by Raman spectroscopy. Phys Rev B 2020;102:24423. https://doi.org/10.1103/PhysRevB.102.024423.

[67] Wu H, Wang L, Wang Y, Guo S, Shen Z. Enhanced microwave performance of highly ordered mesoporous carbon coated by Ni 2O 3 nanoparticles. J Alloys Compd 2012;525:82–6. https://doi.org/10.1016/j.jallcom.2012.02.078.

[68] Šćepanović M, Grujić-Brojčin M, Vojisavljević K, Bernik S, Srećković T. Raman study of structural disorder in ZnO nanopowders. J Raman Spectrosc 2010;41:914–21. https://doi.org/10.1002/jrs.2546.

[69] Srivastava V, Gusain D, Sharma YC. Synthesis, characterization and application of zinc oxide nanoparticles (n-ZnO). Ceram Int 2013;39:9803–8. https://doi.org/10.1016/j.ceramint.2013.04.110.

[70] Xu JF, Ji W, Shen ZX, Tang SH, Ye XR, Jia DZ, et al. Preparation and characterization of CuO nanocrystals. J Solid State Chem 1999;147:516–9. https://doi.org/10.1006/jssc.1999.8409.

[71] Rashad M, Rüsing M, Berth G, Lischka K, Pawlis A. CuO and Co_3O_4 nanoparticles: synthesis, characterizations, and Raman spectroscopy. J Nanomater 2013;2013:714853. https://doi.org/10.1155/2013/714853.

[72] Mironova-Ulmane N, Kuzmin A, Sildos I, Pärs M. Polarisation dependent Raman study of single-crystal nickel oxide. Cent Eur J Phys 2011;9:1096–9. https://doi:10.2478/s11534-010-0130-9.

[73] Srnanek R, Hotovy I, Malcher V, Vincze A, McPhail D, Littlewood S. A Raman study of NiO/sub x/films for gas sensors applications. ASDAM 2000. Conference

proceedings. Third international EuroConference on advanced semiconductor devices and microsystems (cat. No.00EX386). 2000. p. 303–6. https://doi.org/10.1109/ASDAM.2000.889506.
[74] Qiao Y, Liu Q, Lu S, Chen G, Gao S, Lu W, et al. High-performance non-enzymatic glucose detection: using a conductive Ni-MOF as an electrocatalyst. J Mater Chem B 2020;8:5411–5. https://doi.org/10.1039/D0TB00131G.
[75] Sun HM, Ye YX, Tian ZF, Wu SL, Liu J, Liang CH. Ni3+ doped cobalt–nickel layered double hydroxides as high-performance electrode materials for supercapacitors. RSC Adv 2017;7:49010–4. https://doi.org/10.1039/C7RA09427B.
[76] Gupta NK, Bae J, Kim S, Kim KS. Fabrication of Zn-MOF/ZnO nanocomposites for room temperature H2S removal: adsorption, regeneration, and mechanism. Chemosphere 2021;274:129789. https://doi.org/10.1016/j.chemosphere.2021.129789.
[77] Tian H, Liu S, Zhang Z, Dang T, Lu Y, Liu S. Highly stable polyoxovanadate-based Zn–MOF with dual active sites as a solvent-free catalyst for C–C bond formation. ACS Sustain Chem Eng 2021;9:4660–7. https://doi.org/10.1021/acssuschemeng.1c00389.
[78] An L, Xu K, Li W, Liu Q, Li B, Zou R, et al. Exceptional pseudocapacitive properties of hierarchical NiO ultrafine nanowires grown on mesoporous NiO nanosheets. J Mater Chem A Mater 2014;2:12799–804. https://doi.org/10.1039/c4ta01595a.
[79] Fan Z, Liang J, Yu W, Ding S, Cheng S, Yang G, et al. Ultrathin NiO nanosheets anchored on a highly ordered nanostructured carbon as an enhanced anode material for lithium ion batteries. Nano Energy 2015;16:152–62. https://doi.org/10.1016/j.nanoen.2015.06.009.
[80] Moeinian M, Akhbari K. Effect of the pillar ligand on preventing agglomeration of ZnO nanoparticles prepared from Zn (II) metal-organic frameworks. Nano Chem Res 2016;1:64–9. https://doi.org/10.7508/ncr.2016.01.008.
[81] Meng X, Bi M, Xiao Q, Gao W. Ultra-fast response and highly selectivity hydrogen gas sensor based on Pd/SnO2 nanoparticles. Int J Hydrogen Energy 2022;47:3157–69. https://doi.org/10.1016/j.ijhydene.2021.10.201.
[82] Mirzaei A, Kim J-H, Kim HW, Kim SS. How shell thickness can affect the gas sensing properties of nanostructured materials: survey of literature. Sens Actuators B Chem 2018;258:270–94. https://doi.org/10.1016/j.snb.2017.11.066.
[83] Choi S-J, Kim I-D. Recent developments in 2D nanomaterials for chemiresistive-type gas sensors. Electron Mater Lett 2018;14:221–60. https://doi.org/10.1007/s13391-018-0044-z.
[84] Kim H-J, Lee J-H. Highly sensitive and selective gas sensors using p-type oxide semiconductors: overview. Sens Actuators B Chem 2014;192:607–27. https://doi.org/10.1016/j.snb.2013.11.005.
[85] Wetchakun K, Samerjai T, Tamaekong N, Liewhiran C, Siriwong C, Kruefu V, et al. Semiconducting metal oxides as sensors for environmentally hazardous gases. Sens Actuators B Chem 2011;160:580–91. https://doi.org/10.1016/j.snb.2011.08.032.
[86] Yuan H, Li N, Fan W, Cai H, Zhao D. Metal-organic framework based gas sensors. Adv Sci 2022;9:2104374. https://doi.org/10.1002/advs.202104374.
[87] Navale S, Shahbaz M, Majhi SM, Mirzaei A, Kim HW, Kim SS. CuxO nanostructure-based gas sensors for H2S detection: an overview. Chemosensors 2021;9:127. https://doi.org/10.3390/chemosensors9060127.
[88] Boroun Z, Ghorbani M, Moosavi A, Mohammadpour R. New insight into H2S sensing mechanism of continuous SnO2–CuO bilayer thin film: a theoretical macroscopic approach. J Phys Chem C 2016;120:7678–84. https://doi.org/10.1021/acs.jpcc.6b01504.
[89] Peng F, Sun Y, Yu W, Lu Y, Hao J, Cong R, et al. Studies on sensing properties and mechanism of Cuo nanoparticles to H2s gas. Nanomaterials 2020;10. https://doi.org/10.3390/nano10040774.
[90] Peng F, Sun Y, Yu W, Lu Y, Hao J, Cong R, et al. Gas sensing performance and mechanism of CuO(P)-WO3(n) composites to H2S gas. Nanomaterials 2020;10:1–15. https://doi.org/10.3390/nano10061162.
[91] Kim J, Kim W, Yong K. CuO/ZnO heterostructured nanorods: photochemical synthesis and the mechanism of H2S gas sensing. J Phys Chem C 2012;116:15682–91. https://doi.org/10.1021/jp302129j.
[92] Kim J-H, Mirzaei A, Woo Kim H, Wu P, Kim SS. Design of supersensitive and selective ZnO-nanofiber-based sensors for H2 gas sensing by electron-beam irradiation. Sens Actuators B Chem 2019;293:210–23. https://doi.org/10.1016/j.snb.2019.04.113.
[93] Dey S, Mehta NS. Oxidation of carbon monoxide over various nickel oxide catalysts in different conditions: a review. Chemical Engineering Journal Advances 2020;1:100008. https://doi.org/10.1016/j.ceja.2020.100008.
[94] Doan TLH, Kim J-Y, Lee J-H, Nguyen LHT, Nguyen HTT, Pham ATT, et al. Facile synthesis of metal-organic framework-derived ZnO/CuO nanocomposites for highly sensitive and selective H2S gas sensing. Sens Actuators B Chem 2021;349:130741. https://doi.org/10.1016/j.snb.2021.130741.
[95] Wang X, Kong D, Li X, Xie K. MOF-derived hierarchical hollow Fe2O3 nanobox functionalized with Ru doping for superior H2S sensing. Colloids Surf A Physicochem Eng Asp 2024;682:132936. https://doi.org/10.1016/j.colsurfa.2023.132936.
[96] Cao S, Zhou T, Xu X, Bing Y, Sui N, Wang J, et al. Metal-organic frameworks derived inverse/normal bimetallic spinel oxides toward the selective VOCs and H2S sensing. J Hazard Mater 2023;457:131734. https://doi.org/10.1016/j.jhazmat.2023.131734.
[97] Tan J, Hussain S, Ge C, Wang M, Shah S, Liu G, et al. ZIF-67 MOF-derived unique double-shelled Co3O4/NiCo2O4 nanocages for superior Gas-sensing performances. Sens Actuators B Chem 2020;303:127251. https://doi.org/10.1016/j.snb.2019.127251.
[98] Shi T, Hou H, Hussain S, Ge C, Alsaiari MA, Alkorbi AS, et al. Efficient detection of hazardous H2S gas using multifaceted Co3O4/ZnO hollow nanostructures. Chemosphere 2022;287:132178. https://doi.org/10.1016/j.chemosphere.2021.132178.
[99] Guo M, Luo N, Bai Y, Xue Z, Hu Q, Xu J. MEMS sensor based on MOF-derived WO3-C/In2O3 heterostructures for hydrogen detection. Sens Actuators B Chem 2024;398:134151. https://doi.org/10.1016/j.snb.2023.134151.
[100] Dong H-D, Zhao J-P, Peng M-X, Zhang Y-H, Xu P-Y. Au-modified spindle ZnO for high efficiency H2 sensors. Vacuum 2023;207:111597. https://doi.org/10.1016/j.vacuum.2022.111597.
[101] Cheng I-K, Lin C-Y, Pan F-M. Gas sensing behavior of ZnO toward H2 at temperatures below 300°C and its dependence on humidity and Pt-decoration. Appl Surf Sci 2021;541:148551. https://doi.org/10.1016/j.apsusc.2020.148551.
[102] Agarwal S, Kumar S, Agrawal H, Moinuddin MG, Kumar M, Sharma SK, et al. An efficient hydrogen gas sensor based on hierarchical Ag/ZnO hollow microstructures. Sens Actuators B Chem 2021;346:130510. https://doi.org/10.1016/j.snb.2021.130510.
[103] Zhong X, Shen Y, Zhao S, Wei D, Zhang Y, Wei K. Hydrothermal growth of overlapping ZnO nanorod arrays on the porous substrate and their H2 gas sensing. Mater Charact 2021;172:110858. https://doi.org/10.1016/j.matchar.2020.110858.
[104] Xie R, Lu J, Liu Y. Carbon monoxide gas sensing properties of SnO2 modified metal-organic skeleton derived NiO. Sens Actuators A Phys 2024;367:115038. https://doi.org/10.1016/j.sna.2024.115038.
[105] Zhao F, Cao W, Wang PH, Wang J, Yu L, Qiao Z, et al. Fast and sensitive detection of CO by Bi-MOF-Derived porous In2O3/Fe2O3 core-shell nanotubes. ACS Sens 2023;8:4577–86. https://doi.org/10.1021/acssensors.3c01500.
[106] Yang Z, Zhang D, Wang D. Carbon monoxide gas sensing properties of metal-organic frameworks-derived tin dioxide nanoparticles/molybdenum diselenide nanoflowers. Sens Actuators B Chem 2020;304:127369. https://doi.org/10.1016/j.snb.2019.127369.
[107] Li S, Wei X, Zhu S, Zhou Q, Gui Y. Low temperature carbon monoxide gas sensor based on Co3O4@TiO2 nanocomposites: theoretical and experimental analysis. J Alloys Compd 2021;882:160710. https://doi.org/10.1016/j.jallcom.2021.160710.
[108] Nakate UT, Patil P, Na S-I, Yu YT, Suh E, Hahn Y-B. Fabrication and enhanced carbon monoxide gas sensing performance of p-CuO/n-TiO2 heterojunction device. Colloids Surf A Physicochem Eng Asp 2021;612:125962. https://doi.org/10.1016/j.colsurfa.2020.125962.